

# *Olbedo*: An Albedo and Shading Aerial Dataset for Large-Scale Outdoor Environments

Shuang Song<sup>a†</sup> Debao Huang<sup>a†</sup> Deyan Deng<sup>a</sup> Haolin Xiong<sup>b</sup> Yang Tang<sup>a</sup>  
Yajie Zhao<sup>b</sup> Rongjun Qin<sup>a\*</sup>

<sup>a</sup> The Ohio State University

<sup>b</sup> University of Southern California

†Contributed equally \* Corresponding author

<https://gdaosu.github.io/olbedo/>



Figure 1. (a) Overview of the *Olbedo* dataset. For each RGB image, *Olbedo* provides ground truth layers for albedo, metric depth, surface normal, sun shading and sky shading. The RGB and albedo layers are stored as HDR images. (b) Relighting 3D models under novel lighting conditions (direction specified by the compass). RGB textures (left) retain shading, causing shadow duplication artifacts, while albedo textures (right) eliminate them for plausible results. Please use Adobe Reader or KDE Okular to view the animations.

## Abstract

*Intrinsic image decomposition (IID) of outdoor scenes is crucial for relighting, editing, and understanding large-scale environments, but progress has been limited by the lack of real-world datasets with reliable albedo and shading supervision. We introduce Olbedo, a large-scale aerial dataset for outdoor albedo–shading decomposition in the wild. Olbedo contains 5,664 UAV images captured across four landscape types, multiple years, and diverse illumination conditions. Each view is accompanied by multi-view consistent albedo and shading maps, metric depth, surface normals, sun and sky shading components, camera poses, and, for recent flights, measured HDR sky domes. These annotations are derived from an inverse-rendering refinement pipeline over multi-view stereo reconstructions and calibrated sky illumination, together with per-pixel confidence masks. We demonstrate that Olbedo enables state-of-the-art diffusion-based IID models, originally trained on synthetic indoor data, to generalize to real outdoor imagery: fine-*

*tuning on Olbedo significantly improves single-view outdoor albedo prediction on the MatrixCity benchmark. We further illustrate applications of Olbedo-trained models to multi-view consistent relighting of 3D assets, material editing, and scene change analysis for urban digital twins. We release the dataset, baseline models, and an evaluation protocol to support future research in outdoor intrinsic decomposition and illumination-aware aerial vision.*

## 1. Introduction

Intrinsic image decomposition (IID) [13, 14], the process of separating an image into its reflectance (albedo) and shading components, is a fundamental, long-standing problem in computer vision and graphics. Recovering intrinsic properties is essential for robust material understanding, physically based rendering, and high-fidelity 3D reconstruction. While deep learning has significantly advanced IID [10, 28, 43, 45], much of this progress remains confined to indoor or synthetic

environments.

The primary barrier to advancing IID for real-world scenarios is the profound difficulty of acquiring dense, high-fidelity ground truth albedo in large-scale outdoor environments. Unlike indoor scenes where lighting can be controlled [33, 47], outdoor scenes are subject to dynamic, complex illumination from the sun and sky. Capturing ground truth albedo in the wild, at scale, has been considered extremely challenging. Consequently, there is no large-scale, real-world dataset to train IID models for complex aerial scenarios, and models trained on synthetic or indoor data often fail to generalize to real aerial imagery.

To bridge this gap, we present *Olbedo*, the first large-scale, real-world dataset specifically designed for albedo recovery in aerial multi-view stereo (MVS). *Olbedo* comprises high-resolution UAV imagery, dense ground-truth albedo and shading maps, and auxiliary geometry and illumination data generated via a physics-based inverse-rendering pipeline [37, 38].

This dataset addresses a bottleneck in 3D content creation: weather-dependent capture bakes illumination into textures, which undermines physically based rendering (PBR) workflows and imposes significant logistical burdens. *Olbedo* provides the supervision needed to learn lighting-invariant reflectance with multi-view consistency, enabling flexible, weather-agnostic capture pipelines.

Using our data set, we adapt three state-of-the-art diffusion-based IID models [20, 21, 45] to single-view outdoor albedo prediction by Low-Rank Adaptation (LoRA) [18] fine-tuning, yielding improved generalization to complex outdoor scenes. Moreover, *Olbedo* complements synthetic datasets in IID: combining synthetic pretraining with *Olbedo* fine-tuning further boosts outdoor albedo inference, as shown in our experiments. Subsequent applications demonstrate benefits for relighting, 3D modeling, and scene understanding.

## 2. Related Work

Our work is positioned at the intersection of IID and methods for creating ground truth albedo datasets. We address a critical gap by providing the first large-scale, real-world dataset for aerial albedo recovery, which has been a major bottleneck for the field.

**Intrinsic Image Decomposition.** IID is a foundational, yet highly ill-posed problem in computer vision [13, 14]. It aims to factor an input image  $I$  into illumination-invariant reflectance (albedo)  $R$  and illumination-variant shading  $S$ , such that  $I = R \cdot S$  [24]. Early approaches relied on hand-crafted priors and optimization frameworks, assuming that shading is spatially smooth while reflectance is piecewise constant [1, 2, 6, 36]. These priors often fail on complex, non-Lambertian surfaces in real scenes [2].

Learning-based approaches have significantly advanced IID by leveraging large datasets to learn complex priors [4, 13]. Convolutional neural networks (CNNs) have been trained to learn these priors directly from data [19]. These methods have evolved across several paradigms. Supervised methods learn a direct mapping from an input image to its decomposed layers but are entirely dependent on large-scale, pixel-aligned ground truth [3, 45]. Self-supervised and unsupervised methods leverage the image formation model itself as a loss, often using reconstruction error to guide training on unlabeled data [43, 44]. More recently, diffusion-based models [10, 20, 22, 45] have achieved state-of-the-art performance by leveraging the rich foundational priors in large diffusion models [31, 34].

**The Ground Truth Dataset Bottleneck.** The primary limitation in IID research is the profound difficulty of acquiring dense, pixel-perfect ground truth for albedo and shading. This challenge has shaped the field, with existing datasets falling into three main categories based on their creation methodology.

- **Synthetic datasets:** To obtain perfect, dense ground truth, many datasets rely on PBR. Key examples include MPI Sintel [7], CGIntrinsics [26], InteriorVerse [47], and Hypersim [33]. While providing high-quality labels, they are often object-centric or indoor-focused and suffer from a significant "sim-to-real" gap. Models trained on them struggle to generalize to the complexity of real-world photography.
- **Real-world controlled datasets:** To capture real-world statistics, some datasets use controlled lab environments. The MIT Intrinsic dataset [15], MID [8, 30], and DIR [11] captured objects or indoor scenes under multiple, known lighting conditions. This multi-illumination data allows for the computation of pseudo-ground truth albedo. However, this methodology is not scalable and is fundamentally restricted to small, indoor environments.
- **Real-world "in-the-wild" datasets:** The Intrinsic Images in the Wild (IIW) dataset [5] provided a leap in scale by collecting real-world images. However, its ground truth consists of sparse, relative human judgments (e.g., "point A is lighter than point B"). It provides no dense albedo maps.

Existing IID methods are limited by datasets that are either (a) synthetic, (b) indoor-only, or (c) lack of dense ground truth. There is a major gap: no large-scale, real-world dataset for intrinsic decomposition in complex, outdoor, aerial environments.

Our work, *Olbedo*, directly addresses this gap by introducing a novel pipeline to generate the first dense, large-scale, real-world ground truth for aerial albedo recovery.

### 3. *Olbedo* Dataset

#### 3.1. Overview

The *Olbedo* dataset provides a large-scale benchmark for albedo-shading decomposition of outdoor aerial imagery in the wild. Our dataset includes decomposed albedo and shading maps as ground truth for each image. We also provide intermediate geometric features, including depth, normals, sun shading, sky shading, and (for recent flights) sky radiance images, to facilitate multi-task learning.

#### 3.2. Data Collection

The *Olbedo* dataset is derived from aerial datasets captured in RAW format, along with a sky radiance image captured simultaneously during drone flights. The sun position is determined from astronomical ephemeris using UTC time and site location; no special instruments are required. Precise 3D geometry is essential for albedo-shading decomposition. Accordingly, we use a photogrammetry pipeline to solve accurate camera poses and reconstruct highly precise surface meshes from our in-house collected, multi-temporal image sets. The image sets include repeated data-collection flights over up to four years. The dataset covers four landscape types, as shown in Fig. 2.

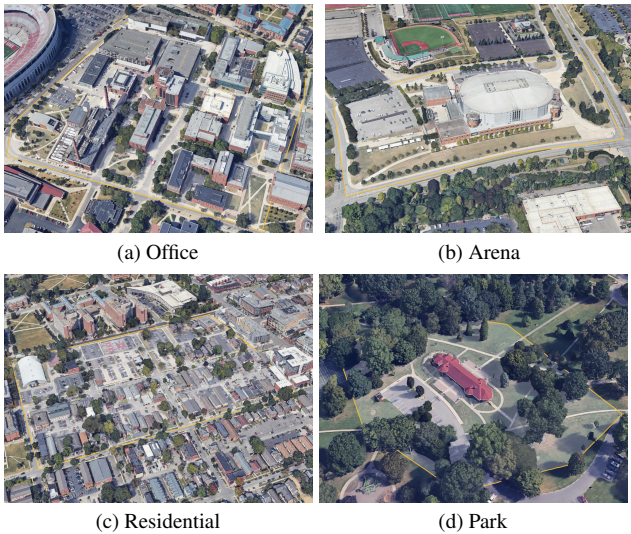
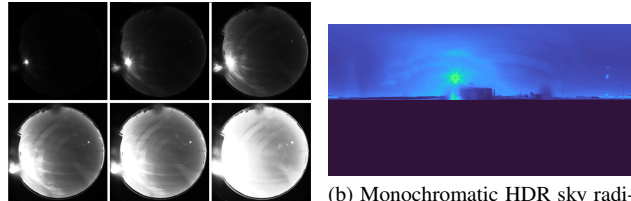


Figure 2. Landscapes of the *Olbedo* dataset. (cr: Google)

**Temporal Image Collection.** We collected aerial images over multiple flights for each scene to cover diverse lighting conditions. Each flight lasts approximately 10 to 25 minutes, depending on site area. For each scene, we conducted 2 to 4 flights at different times of day across multiple years to capture the scene under varying illumination. Each flight captures around 50 to 230 images with 80% forward and side overlap to ensure robust reconstruction. The images are captured in a nadir view with slight oblique angles to cover vertical surfaces.

**Sky Radiance Capture.** For flights in 2025, we capture an

HDR all-sky radiance dome with a  $180^\circ$  fisheye rig (Sony ExView II CCD, IR and ND filters). Each sequence brackets 11 exposures (0.5–32 s) recorded as 16-bit FITS and merged into a 32-bit EXR radiance map following [12]. The sky camera is aligned to the world frame via surveyed control points (GNSS RTK/total station), and the dome is provided in equirectangular format, as shown in Fig. 3. We use luminance-only sky domes to model  $S_{sky}$  and ephemeris-based sun direction for  $S_{sun}$ . Sky radiance maps and meta-data are released per flight; when sky radiance is unavailable, an analytic sky model can be applied.



(a) Exposure-bracketed raw sky frames (0.5–32 s). (b) Monochromatic HDR sky radiance image in equirectangular projection.

Figure 3. Sky radiance acquisition and representation. Left: exposure-bracketed raw sky images. Right: merged HDR sky dome in equirectangular format.

**Statistics and Coverage.** Fig. 4 summarizes dataset statistics, including the distribution of images by year, scene type, and weather condition. Our dataset has 5,664 images from 2022 to 2025, covering four landscape types: office, arena, residential, and natural park. Weather conditions include clear-sky sunrise/sunset and overcast days.

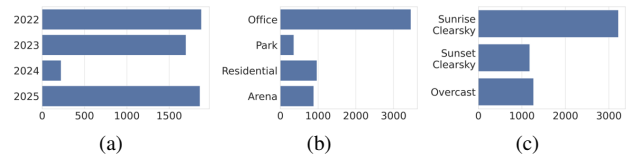


Figure 4. Statistics of our multi-temporal albedo dataset. (a) Distribution of images per year. (b) Distribution of images per site. (c) Distribution of images per lighting condition.

#### 3.3. Ground-truth Albedo Curation

Decomposing albedo from images is a central challenge in developing our dataset. Our dataset builds on a multi-view albedo-shading decomposition method that estimates outdoor shading from a single temporal sample. It requires linear radiance images, accurate geometry, precise image poses, and sun position as inputs to separate albedo from shading.

**Aerial Image Preprocessing.** We use a DJI Phantom 4 Pro V2.0 with a 1-inch CMOS camera and capture RAW (DNG) only. In-camera JPEGs are *not* used because they apply a tone curve, gamma, and other vendor processing that destroy the linear relationship between the radiance and the pixel values. This is required by the albedo-shading decomposition method[38]. We read DNGs with OpenImageIO configured for RAW output in linear camera space (e.g.,

*oii:RawColor=1, raw:ColorSpace=Linear*). No JPEG path, tone mapping, or gamma/CRF is applied. All released RGB, albedo, and shading images remain in linear color space. sRGB is used only for figures in the paper and preview thumbnails. The camera poses, intrinsics and high-quality 3D geometry are solved by a commercial photogrammetry software (Bentley iTwin Capture<sup>1</sup>). We provide per-image metadata linking sources to converted EXRs including camera intrinsics/poses. The geo-registered images are downsampled 8 times to 683×455 resolution for image decomposition processing. For more details, please refer to our supplementary Sec. A.

**Image Decomposition Framework.** Our method follows [37, 38], a physics-based outdoor intrinsic image decomposition approach. The key idea is to model and estimate shading by solving for a sun–sky illumination model. The method relies on pairs of pixels near shadow boundaries that share approximately the same albedo. The image formation model is defined in Eq. (1).

$$I = R \odot (\phi \odot S_{sun} + S_{sky}) \quad (1)$$

where  $I$  is a linear radiance image,  $R$  is the albedo (reflectance), and  $S_{sun}$  and  $S_{sky}$  are the normalized sun and sky shading components, and  $\odot$  denotes channel-wise multiplication. These shading terms are derived from geometric features such as surface normals, sun visibility, and sky visibility [38]. The sun-visibility term, i.e., the cast-shadow map, is also used to find lit–shadow pixel pairs. These pairs are automatically detected and filtered by normal difference, depth difference, and a brightness threshold. As illustrated in Fig. 5, we assume that the albedo is approximately uniform within a local region; thus a lit–shadow pixel pair shares the same albedo. The derivation is shown in Eq. (2). Finally, we estimate the optimal  $\phi$ , the ratio between sun and sky illumination, from all sunlit pairs in an image using a Gaussian Mixture Model (GMM). The GMM has two components that model the actual distribution of  $\phi$  and the noise distribution, both assumed to be Gaussian but with very different variances. For detailed definitions of these two components, please refer to our supplementary material in Sec. B.

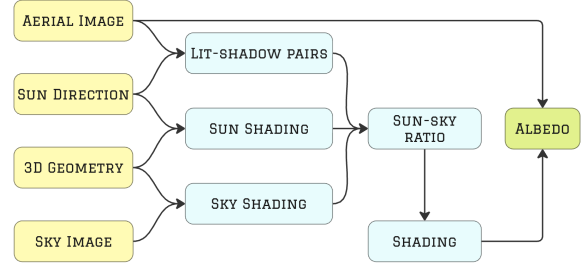
$$\begin{aligned} \frac{I_{lit} - I_{shadow}}{I_{shadow}} &= \frac{(\phi \odot S_{sun} + S_{sky} - S_{sky}) \odot R}{S_{sky} \odot R} \\ \implies \phi &= \frac{S_{sky} \odot (I_{lit} - I_{shadow})}{S_{sun} \odot I_{shadow}} \end{aligned} \quad (2)$$

where  $I_{lit}$  and  $I_{shadow}$  are the pixel values of the lit and shadowed regions, respectively. Once  $\phi$  is estimated, we compute the albedo with Eq. (3):

$$R = \frac{I}{\phi \odot S_{sun} + S_{sky}} \quad (3)$$

<sup>1</sup><https://www.bentley.com/software/itwin-capture/>

Because  $\phi$  is the ratio between sun and sky illumination, the recovered albedo is defined only up to a global scale, which is not observable in this decomposition framework. However, this does not affect the effectiveness of using the decomposed albedo to train learning-based albedo–shading models, as demonstrated in Sec. 4. We find that the trained model does not strictly require RAW inputs; the results in Sec. 5 are produced from linearized sRGB images.



(a) Yellow boxes represent data sources, blue boxes indicate intermediate processing, and the green box is the final product.



(b) Lit-shadow pair in image,  $\phi$  is a ratio between sun and sky shading.

Figure 5. Our image decomposition framework.

By default (Fig. 5a), we compute sky shading  $S_{sky}$  with a *uniform sky lighting* model[38]. When an HDR sky camera is available (our 2025 flights), we replace the uniform dome with the measured sky radiance map to capture subtle anisotropy (e.g., horizon brightening, partial clouds). Because the measured sky radiance maps are not aligned with the estimated shading terms, we first solve the uniform sky-lighting model for each flight to establish a global scale, then align the measured sky radiance to this model via a least-squares gain before evaluating  $S'_{sky}$ . This preserves the decomposition scale while injecting real sky detail where available.

**Confidence Masks.** To facilitate network training, we curate per-pixel confidence masks for the decomposed albedo. The confidence accounts for two error sources in the decomposition: (1) geometric errors from photogrammetry (less-accurate surfaces near mesh boundaries); and (2) the sun-visibility mask cast by the reconstructed geometry, for which shadow boundaries may be noisy due to imperfect geometry. We dilate geometric-error regions and shadow boundaries to generate a binary confidence mask. The confidence masks are released alongside the albedo and shading

maps in our dataset. An example of the confidence mask is shown in our supplementary Sec. C.

**Validation.** Validating ground truth is essential for building a reliable dataset. However, measuring ground-truth albedo, especially outdoors and from UAV viewpoints, is very challenging. Therefore, we validate our decomposed albedo from two aspects: (1) we fine-tune recent albedo-shading decomposition networks on our dataset and evaluate them on synthetic datasets with ground-truth albedo to demonstrate training effectiveness (see Sec. 4); and (2) we present applications using the decomposed albedo (e.g., relighting, texture editing, and change detection) to demonstrate the capability of models trained on our dataset (see Sec. 5).

## 4. Experiments

In this section, we evaluate the effectiveness of the *Olbedo* dataset for single-view outdoor albedo estimation. To this end, we fine-tune state-of-the-art IID methods on the *Olbedo* dataset and compare their performance with that of the corresponding pretrained models.

### 4.1. Baselines

Recent advances in IID have shifted toward leveraging foundation models, such as large diffusion models [31, 34], which provide rich visual priors learned from massive image-text datasets [35]. By fine-tuning these pretrained models, recent approaches have demonstrated promising results in single-view indoor albedo estimation. Accordingly, we select three diffusion-based approaches: Intrinsic Image Diffusion [21], RGB $\leftrightarrow$ X [45], and Marigold-IID-Appearance [20] for evaluation. These methods represent the current state-of-the-art in IID for indoor scenes. Intrinsic Image Diffusion and Marigold-IID-Appearance are trained on the synthetic InteriorVerse dataset [47], whereas RGB $\leftrightarrow$ X is further trained on additional synthetic data from Hypersim [33] and self-constructed Evermotion datasets, which contain heterogeneous intrinsic properties. RGB $\leftrightarrow$ X manages multiple modalities by employing the text encoder as a switch to control the desired output.

### 4.2. Fine-tuning using *Olbedo*

We fine-tune these models for outdoor albedo estimation using the entire *Olbedo* dataset. Since the original models are trained on synthetic indoor datasets containing multiple modalities, we specifically fine-tune the channel corresponding to albedo prediction. For Intrinsic Image Diffusion and Marigold-IID-Appearance, we retain only the albedo channel during fine-tuning. In the case of RGB $\leftrightarrow$ X, we fix the text prompt to “albedo” to guide the model toward the desired output.

Given the relatively small size of the *Olbedo* dataset compared to the synthetic indoor datasets used by the selected

models, we adopt Low-Rank Adaptation (LoRA) [18] for fine-tuning. We employ LoRA instead of full fine-tuning to mitigate the risk of overfitting and to reduce both memory consumption and computational cost. This approach preserves the generalizability of the pretrained model while enabling it to learn the new task of single-view outdoor albedo prediction.

Specifically, LoRA is applied to the query, key, value, and output projection matrices within the attention modules of the U-Net across all models. The number of trainable parameters for all models is approximately 1.66 M, representing only 0.19% of the total U-Net parameters. For Intrinsic Image Diffusion, we also fine-tune the custom latent encoder, as we find that the pretrained encoder exhibits limited generalization to outdoor images. During LoRA fine-tuning, we reduce the number of epochs to three and set the learning rate to 5e-6 for Intrinsic Image Diffusion and Marigold-IID-Appearance, and 5e-7 for RGB $\leftrightarrow$ X. All other training settings are adopted from the respective original models.

### 4.3. Evaluation

**Evaluation Datasets.** We evaluate both the fine-tuned and pretrained models on the MatrixCity benchmark [25]. This large-scale synthetic outdoor dataset enables the rendering of various scene properties, including depth, normals, and albedo, within city-scale environments. We use MatrixCity to assess whether the fine-tuned models have learned the albedo and shading priors for outdoor scenarios from our *Olbedo* dataset. Using the provided plugin, we capture RGB images under different lighting and shading conditions and generate the corresponding albedo images as ground truth. The evaluation dataset comprises a total of 520 images at a resolution of 1920  $\times$  1080, covering a wide range of scene layouts and lighting variations, thereby providing a representative test set.

**Evaluation Protocol.** We use the original inference settings of each method to predict albedo for both the fine-tuned and pretrained models. Due to GPU memory limitations, images are resized so that the longer edge is 1000 pixels for all models, while preserving the aspect ratio. Following the evaluation protocols in [20, 45], the predicted albedo is resized back to the original resolution and compared directly with the ground truth without any alignment. The reported evaluation metrics include Peak Signal-to-Noise Ratio (PSNR), Structural Similarity Index Measure (SSIM) [39], and Learned Perceptual Image Patch Similarity (LPIPS) [46].

**Quantitative Evaluation.** As shown in Tab. 1, all models achieve consistent improvements across all evaluation metrics after fine-tuning on our *Olbedo* dataset. Intrinsic Image Diffusion achieves PSNR, SSIM, and LPIPS improvements of 10.6%, 7.7%, and 12.5%, respectively. Marigold-IID-Appearance shows the largest gains, with PSNR increasing

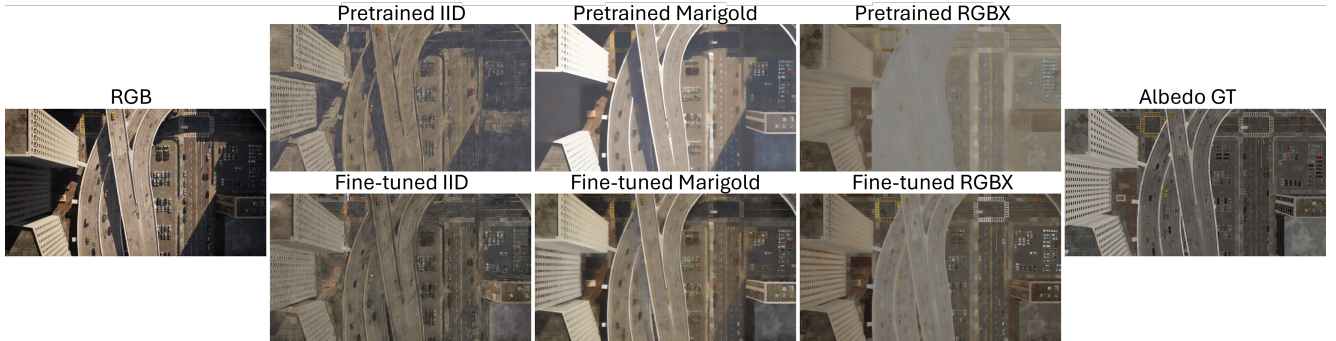


Figure 6. Qualitative comparison of fine-tuned and pretrained models for outdoor albedo prediction on the MatrixCity dataset. IID = Intrinsic Image Diffusion [21], Marigold = Marigold-IID-Appearance [20], RGBX = RGB $\leftrightarrow$ X [45].

Table 1. Quantitative comparison of fine-tuned and pretrained models for outdoor albedo prediction on the MatrixCity dataset. IID = Intrinsic Image Diffusion [21], Marigold = Marigold-IID-Appearance [20], RGBX = RGB $\leftrightarrow$ X [45].

Model	PSNR $\uparrow$	SSIM $\uparrow$	LPIPS $\downarrow$
Pretrained IID	15.594	0.493	0.554
Fine-tuned IID	<b>17.249</b>	<b>0.531</b>	<b>0.485</b>
Pretrained Marigold	10.153	0.508	0.591
Fine-tuned Marigold	<b>17.118</b>	<b>0.570</b>	<b>0.461</b>
Pretrained RGBX	15.050	0.559	0.472
Fine-tuned RGBX	<b>17.735</b>	<b>0.611</b>	<b>0.413</b>

by 68.6%, SSIM by 12.2%, and LPIPS decreasing by 22.0%. For RGB $\leftrightarrow$ X, PSNR increases by approximately 17.8%, SSIM by 9.3%, and LPIPS decreases by 12.5%. These results demonstrate that fine-tuning, even with a small dataset using LoRA, substantially improves both the pixel-level accuracy and perceptual quality of single-view outdoor albedo predictions.

**Qualitative Evaluation.** As shown in Fig. 6, the pretrained RGB $\leftrightarrow$ X model demonstrates the best performance in shading removal compared to the other two pretrained models, benefiting from training on larger datasets. However, this comes at the cost of losing fine details. Flattened, indoor-style texture are observed in all the pretrained models. The fine-tuned models exhibit noticeable visual improvements, effectively reducing shading artifacts for Marigold-IID-Appearance and Intrinsic Image Diffusion. In addition, the colors align more closely with ground truth albedo, and more details are recovered, such as vehicles, lane lines, and building textures. Overall, the fine-tuned RGB $\leftrightarrow$ X achieves the best qualitative performance, consistent with the quantitative results reported in Tab. 1.

## 5. Applications

In this section, we present several applications of albedo prediction using the fine-tuned models, highlighting the prac-

tical value of our *Olbedo* dataset. For these applications, we use the fine-tuned RGB $\leftrightarrow$ X model to generate the albedo, as it achieves the best performance in both quantitative and qualitative evaluations in Sec. 4.3.



Figure 7. Predicted albedo images of the Gazebo scene from the BlendedMVS dataset, obtained from the fine-tuned RGB $\leftrightarrow$ X model using *Olbedo*.

### 5.1. Multi-view Consistent Relighting

In the creation of urban digital twins, UAV or aerial image acquisition is often conducted under overcast conditions to avoid strong shading effects that can interfere with downstream data exploitation and interpretation [27, 29]. By predicting albedo images using our fine-tuned models, most shading effects can be effectively removed. This enables more flexible post-processing and reduces the constraints imposed by weather and lighting conditions on data collection.

We first demonstrate the multi-view consistency of the predicted albedo. Experiments are conducted on the publicly available large-scale MVS dataset, BlendedMVS [41]. As shown in Fig. 7, albedo generated by the fine-tuned RGB $\leftrightarrow$ X model effectively removes shading effects from the RGB images. More importantly, the recovered albedo remains consistent across multiple views, allowing it to be textured onto the 3D model and facilitating downstream relighting applications that require a base model with view-invariant appearance. Retexturing results are provided in the supplementary Sec. D.

**Relighting.** One important downstream task is the realis-

tic rendering of reconstructed models under novel lighting conditions. To this end, we use a commercial rendering software<sup>2</sup> to render scenes under various lighting and weather conditions. As shown in Fig. 8, rendering with the original RGB texture under novel illumination results in lighting inconsistency and violates physical plausibility, since the original shading is already baked into the texture. For example, shadow duplication can occur under sunny conditions when the lighting direction differs from that of the original data capture. Additionally, shadows may appear counterintuitively under rainy conditions. In contrast, retextured models using the predicted albedo produce more realistic renderings with reasonable lighting and shading effects across different conditions. These results demonstrate that albedo enables weather- and lighting-independent 3D reconstruction, allowing realistic relighting for practical applications such as digital twin simulation in VR/AR and scene synthesis without the need to re-collect data. Additional results are provided in the supplementary Sec. E.

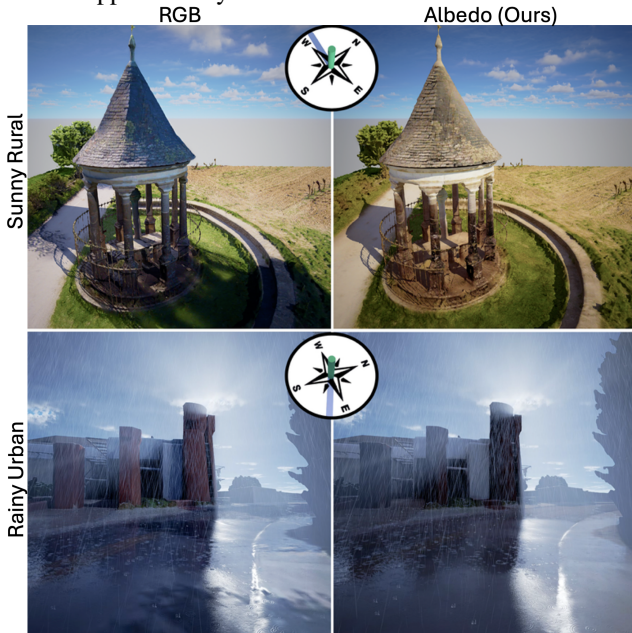


Figure 8. Comparison between RGB textures (left) and our albedo results (right). In the Sunny Rural scene, the RGB textures show roof shadows that suggest illumination toward the viewer, whereas our albedo removes these shadows and correctly reflects lighting from the opposite direction, as indicated by the compass. In the Rainy Urban scene, sunlight comes towards the viewer’s side, yet the RGB-textured model shows tree shadows on the ground and shadows on building facade caused by a different sun direction.

## 5.2. Segmentation on Albedo Image

In this section, we explore the use of albedo images as input for segmentation tasks. Conventional RGB imagery often exhibits complex illumination effects, such as shadows, highlights, and color shifts caused by uneven lighting that can

potentially compromise the model’s ability to consistently extract object boundaries. Modern segmentation models, including Mask R-CNN [16], DeepLabv3 [9], and Segment Anything Model (SAM) [32], typically rely on spatial continuity and texture contrast to infer region boundaries. However, shadows introduce artificial edges and abrupt intensity transitions that do not correspond to real object boundaries. This misleads models into interpreting illumination differences as structural cues, causing over-segmentation or inaccurate delineation of shaded regions. Albedo images, in contrast, capture only the intrinsic surface reflectance, independent of lighting, thereby mitigating these inconsistencies. This allows segmentation networks to focus on true material and geometric features rather than transient lighting effects. Consequently, models operating on albedo images can better preserve object coherence and achieve higher consistency across scenes with varying illumination conditions. Using SAM with the same POI (Point of Interest) as a case study, Fig. 9 illustrates that segmentation based on the albedo image produces more stable and continuous masks, particularly in regions where shadows occupy a larger area than the object itself. Additional results are provided in the supplementary Sec. F.

## 5.3. Material Editing

In this section, we introduce a simple yet effective material editing workflow, which leverages intrinsic image decomposition to achieve lighting-consistent color modifications. After predicting the albedo using our fine-tuned RGB $\leftrightarrow$ X model, we further decompose shading using inverse Retinex equation  $S = \frac{I}{R}$ . The edited albedo is then recombined with the original shading to preserve consistent lighting. We compare our method against four baselines: naive alpha-blending, a state-of-the-art diffusion-based method in academia named FlowEdit [23] with a Stable Diffusion 3 [34] (SD3) backbone, and two commercial AI editing tools, Nano Banana [42] and Qwen Image Edit [40].

As shown in Fig. 10, naive alpha blending produces flat, low-contrast results in which the original lighting cues are lost. The FlowEdit + SD3 model, while capable of generating semantically coherent edits, is highly sensitive to text prompts and often over-modifies geometry or textures even when the prompt specifies only color changes. In contrast, Nano Banana and Qwen Image Edit produce visually appealing and realistic results but tend to alter high-frequency details such as roof tiles and brick patterns. Another major limitation of nearly all current AIGC methods is their restriction to specific, low resolutions, which further leads to over-smoothed details. This loss of fine structure results in perceptually pleasing yet physically inconsistent outputs that are unsuitable for downstream tasks such as 3D reconstruction or photometric analysis. By explicitly modeling the albedo–shading relationship, our recoloring workflow

<sup>2</sup><https://www.d5render.com/>

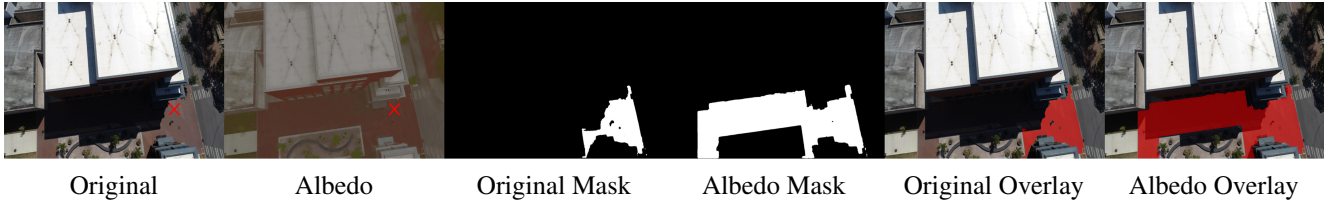


Figure 9. Comparison of segmentation results using SAM [32] on RGB and albedo images. From left to right, each column shows: (1) the original RGB image, (2) the predicted albedo (shadow-free) image, (3) the segmentation mask from SAM using the RGB as input, (4) the segmentation mask from SAM using the albedo as input, and (5-6) the corresponding masks overlaid on the RGB image. The red crosses mark the point of interest (POI) used to guide segmentation across both modalities.



Figure 10. Comparison of material editing results across different methods on an aerial scene. The target colors is ■ (RGB: 40, 0, 0). Naive alpha-blending produces dull and flattened lighting, and AI-Generated Content (AIGC) often alters global illumination or distorts texture. Our material editing workflow, based on intrinsic decomposition and shading reapplication, preserves realistic lighting and surface details, achieving consistent and photometrically coherent edits.

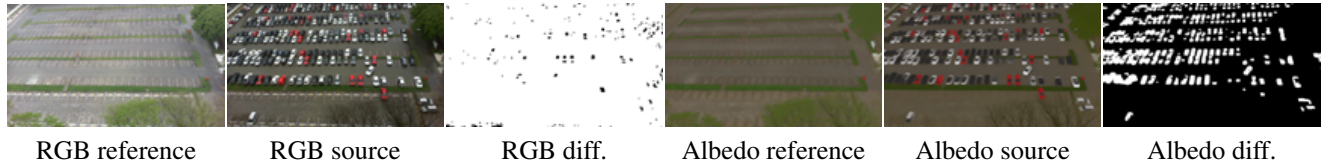


Figure 11. Lighting-invariant scene change analysis using a fixed surveillance camera. The left three columns show the reference and source frames in RGB, along with the naive RGB difference. The right three columns show the reference and source frames in albedo, together with the albedo-based difference. Albedo differencing substantially reduces false positives caused by different illumination conditions, while effectively isolating true scene changes.

preserves both global illumination and local texture fidelity, producing edits that are visually natural and physically consistent for a wide range of downstream computational applications. Additional results are provided in the supplementary Sec. G.

#### 5.4. Scene Change Analysis with Fixed Cameras

We demonstrate how albedo recovery converts fragile pixel-wise differencing into a robust tool for long-term outdoor monitoring with fixed cameras. The core challenge in outdoor scene change analysis is illumination: time-of-day, cast shadows, and weather cause large appearance shifts, making naive RGB differencing unreliable. By predicting albedo with our fine-tuned RGB $\leftrightarrow$ X model, we remove shading effects and substantially stabilize the background.

We use a public parking-lot surveillance dataset captured by a stationary camera [17]. A clean, car-free frame serves as the reference. For each incoming frame  $I_t$ , we compute albedo  $A_t = f(I_t)$ . We then convert both  $A_t$  and  $A_{ref}$  to grayscale and compute a per-pixel difference map  $\Delta_t = |\text{gray}(A_t) - \text{gray}(A_{ref})|$ . A fixed global threshold of 30 is applied to  $\Delta_t$  to obtain a binary change mask, followed by small-blob removal and an *opening* operation for morpho-

logical opening. This simple pipeline yields accurate masks of parked vehicles and other scene changes shown in Fig. 11. Additional results are provided in the supplementary Sec. H. We compare against naive RGB differencing using the same pipeline, which produces many false positives from shadows and lighting changes. Albedo differencing dramatically improves robustness to illumination while isolating true scene changes.

## 6. Conclusion

We introduce *Olbedo*, a large-scale real-world aerial dataset with dense, multi-view consistent albedo and shading, geometry, camera poses, and HDR sky domes for outdoor intrinsic image decomposition. Fine-tuning recent diffusion IID models with lightweight LoRA on *Olbedo* improves single-view outdoor albedo estimation on MatrixCity (PSNR/SSIM/LPIPS) and yields multi-view consistent predictions that enable relighting, segmentation, material editing, and scene change analysis. Crucially, *Olbedo* complements synthetic datasets: combining *Olbedo* with synthetic training data transfers strong indoor/synthetic priors to real outdoor imagery and significantly boosts generalization, as confirmed by our experiments. We will release the dataset, baselines, and evaluation protocol to support research on

outdoor albedo inference and 3D content creation.

## Acknowledgement

This work is supported by the Office of Naval Research (Award No. N000142312670) and Intelligence Advanced Research Projects Activity (IARPA) via Department of Interior/ Interior Business Center (DOI/IBC) contract number 140D0423C0075.

## References

- [1] Jonathan T. Barron and Jitendra Malik. Color constancy, intrinsic images, and shape estimation. In *Proceedings of the 12th European Conference on Computer Vision - Volume Part IV*, pages 57–70, Berlin, Heidelberg, 2012. Springer-Verlag. 2
- [2] Jonathan T. Barron and Jitendra Malik. Shape, albedo, and illumination from a single image of an unknown object. In *2012 IEEE Conference on Computer Vision and Pattern Recognition*, pages 334–341, 2012. 2
- [3] Anil S. Baslamisli, Thomas T. Groenestegge, Partha Das, Hoang-An Le, Sezer Karaoglu, and Theo Gevers. Joint Learning of Intrinsic Images and Semantic Segmentation. In *Proceedings of the European Conference on Computer Vision (ECCV)*, pages 286–302, 2018. 2
- [4] Anil S. Baslamisli, Partha Das, Hoang-An Le, Sezer Karaoglu, and Theo Gevers. ShadingNet: Image Intrinsic by Fine-Grained Shading Decomposition. *International Journal of Computer Vision*, 129(8):2445–2473, 2021. 2
- [5] Sean Bell, Kavita Bala, and Noah Snavely. Intrinsic images in the wild. *ACM Transactions on Graphics*, 33(4):159:1–159:12, 2014. 2
- [6] Adrien Bousseau, Frédo Durand, Frédo Durand, and Sylvain Paris. User-Assisted Intrinsic Images. *ACM Transactions on Graphics*, 28(5), 2009. 2
- [7] Daniel J. Butler, Jonas Wulff, Garrett B. Stanley, and Michael J. Black. A Naturalistic Open Source Movie for Optical Flow Evaluation. In *Computer Vision – ECCV 2012*, pages 611–625, Berlin, Heidelberg, 2012. Springer. 2
- [8] Chris Careaga and Yağız Aksoy. Intrinsic image decomposition via ordinal shading. *ACM Trans. Graph.*, 2023. 2
- [9] Liang-Chieh Chen, George Papandreou, Florian Schroff, and Hartwig Adam. Rethinking atrous convolution for semantic image segmentation. *arXiv preprint arXiv:1706.05587*, 2017. 7
- [10] Xi Chen, Sida Peng, Dongchen Yang, Yuan Liu, Bowen Pan, Chengfei Lv, and Xiaowei Zhou. IntrinsicAnything: Learning diffusion priors for inverse rendering under unknown illumination. In *Computer vision – ECCV 2024: 18th european conference, milan, italy, september 29–october 4, 2024, proceedings, part LX*, pages 450–467, Milan, Italy, 2024. Springer-Verlag. Number of pages: 18 tex.address: Berlin, Heidelberg. 1, 2
- [11] Seokjun Choi, Hoon-Gyu Chung, Yujin Jeon, Giljoo Nam, and Seung-Hwan Baek. A real-world display inverse rendering dataset. In *Proceedings of the IEEE/CVF international conference on computer vision (ICCV)*, pages 25272–25283, 2025. 2
- [12] Paul E. Debevec and Jitendra Malik. Recovering high dynamic range radiance maps from photographs. In *Proceedings of the 24th Annual Conference on Computer Graphics and Interactive Techniques*, pages 369–378, USA, 1997. ACM Press/Addison-Wesley Publishing Co. 3
- [13] Qingnan Fan, Jiaolong Yang, Gang Hua, Baoquan Chen, and David Wipf. Revisiting deep intrinsic image decompositions. In *Proceedings of the IEEE conference on computer vision and pattern recognition (CVPR)*, 2018. 1, 2
- [14] Elena Garcés, Carlos Rodríguez-Pardo, Dan Casas, and Jorge Lopez-Moreno. A Survey on Intrinsic Images: Delving Deep into Lambert and Beyond. *International Journal of Computer Vision*, 130(3):836–868, 2022. 1, 2
- [15] Roger Grosse, Micah K Johnson, Edward H Adelson, and William T Freeman. Ground truth dataset and baseline evaluations for intrinsic image algorithms. In *2009 IEEE 12th International Conference on Computer Vision*, pages 2335–2342, Kyoto, 2009. IEEE. 2
- [16] Kaiming He, Georgia Gkioxari, Peter Dollar, and Ross B. Girshick. Mask r-cnn. In *Proceedings of the IEEE International Conference on Computer Vision (ICCV)*, 2017. 7
- [17] Meng-Ru Hsieh, Yen-Liang Lin, and Winston H. Hsu. Drone-based object counting by spatially regularized regional proposal network. In *Proceedings of the IEEE International Conference on Computer Vision (ICCV)*, 2017. 8, 3
- [18] Edward J Hu, Yelong Shen, Phillip Wallis, Zeyuan Allen-Zhu, Yuanzhi Li, Shean Wang, Lu Wang, Weizhu Chen, et al. Lora: Low-rank adaptation of large language models. *ICLR*, 1(2):3, 2022. 2, 5
- [19] Carlo Innamorati, Tobias Ritschel, Tim Weyrich, and Niloy J. Mitra. Decomposing Single Images for Layered Photo Retouching. *Computer Graphics Forum*, 36(4):15–25, 2017. 2
- [20] Bingxin Ke, Kevin Qu, Tianfu Wang, Nando Metzger, Shengyu Huang, Bo Li, Anton Obukhov, and Konrad Schindler. Marigold: Affordable Adaptation of Diffusion-Based Image Generators for Image Analysis, 2025. arXiv:2505.09358 [cs] version: 1. 2, 5, 6
- [21] Peter Kocsis, Vincent Sitzmann, and Matthias Nießner. Intrinsic image diffusion for indoor single-view material estimation. In *Proceedings of the IEEE/CVF Conference on Computer Vision and Pattern Recognition (CVPR)*, pages 5198–5208, 2024. 2, 5, 6
- [22] Peter Kocsis, Vincent Sitzmann, and Matthias Nießner. Intrinsic Image Diffusion for Single-view Material Estimation. In *CVPR*, 2024. 2
- [23] Vladimir Kulikov, Matan Kleiner, Inbar Huberman-Spiegelglas, and Tomer Michaeli. Flowedit: Inversion-free text-based editing using pre-trained flow models. In *Proceedings of the IEEE/CVF International Conference on Computer Vision*, pages 19721–19730, 2025. 7, 6
- [24] E. H. Land and J. J. McCann. Lightness and retinex theory. *Journal of the Optical Society of America*, 61(1), 1971. 2
- [25] Yixuan Li, Lihan Jiang, Linning Xu, Yuanbo Xiangli, Zhenzhi Wang, Dahua Lin, and Bo Dai. MatrixCity: A Large-scale

- City Dataset for City-scale Neural Rendering and Beyond. In *Proceedings of the IEEE/CVF International Conference on Computer Vision*, pages 3205–3215, 2023. 5
- [26] Zhengqi Li and Noah Snavely. CGIntrinsics: Better Intrinsic Image Decomposition Through Physically-Based Rendering. In *Lecture Notes in Computer Science (Including Subseries Lecture Notes in Artificial Intelligence and Lecture Notes in Bioinformatics)*, 2018. 2
- [27] Liqiang Lin, Yilin Liu, Yue Hu, Xingguang Yan, Ke Xie, and Hui Huang. Capturing, Reconstructing, and Simulating: The UrbanScene3D Dataset. In *Computer Vision – ECCV 2022*, pages 93–109, Cham, 2022. Springer Nature Switzerland. 6
- [28] Yehonathan Litman, Or Patashnik, Kangle Deng, Aviral Agrawal, Rushikesh Zawat, Fernando De la Torre, and Shubham Tulsiani. MaterialFusion: Enhancing Inverse Rendering with Material Diffusion Priors. In *2025 International Conference on 3D Vision (3DV)*, pages 802–812, 2025. 1
- [29] Shuang Luo, Huifang Li, and Huanfeng Shen. Deeply supervised convolutional neural network for shadow detection based on a novel aerial shadow imagery dataset. *ISPRS Journal of Photogrammetry and remote sensing*, 167:443–457, 2020. 6
- [30] Lukas Murmann, Michael Gharbi, Miika Aittala, and Fredo Durand. A multi-illumination dataset of indoor object appearance. In *Proc. ICCV*, 2019. 2
- [31] Aditya Ramesh, Prafulla Dhariwal, Alex Nichol, Casey Chu, and Mark Chen. Hierarchical text-conditional image generation with clip latents. *arXiv preprint arXiv:2204.06125*, 1(2): 3, 2022. 2, 5
- [32] Nikhila Ravi, Valentin Gabeur, Yuan-Ting Hu, Ronghang Hu, Chaitanya Ryali, Tengyu Ma, Haitham Khedr, Roman Rädle, Chloe Rolland, Laura Gustafson, Eric Mintun, Junting Pan, Kalyan Vasudev Alwala, Nicolas Carion, Chao-Yuan Wu, Ross Girshick, Piotr Dollár, and Christoph Feichtenhofer. SAM 2: Segment Anything in Images and Videos, 2024. 7, 8, 3
- [33] Mike Roberts, Jason Ramapuram, Anurag Ranjan, Atulit Kumar, Miguel Angel Bautista, Nathan Paczan, Russ Webb, and Joshua M. Susskind. Hypersim: a photorealistic synthetic dataset for holistic indoor scene understanding. In *Proceedings of the IEEE/CVF international conference on computer vision (ICCV)*, pages 10912–10922, 2021. 2, 5
- [34] Robin Rombach, Andreas Blattmann, Dominik Lorenz, Patrick Esser, and Björn Ommer. High-resolution image synthesis with latent diffusion models, 2021. 2, 5, 7
- [35] Christoph Schuhmann, Romain Beaumont, Richard Vencu, Cade Gordon, Ross Wightman, Mehdi Cherti, Theo Coombes, Aarush Katta, Clayton Mullis, Mitchell Wortsman, et al. Laion-5b: An open large-scale dataset for training next generation image-text models. *Advances in neural information processing systems*, 35:25278–25294, 2022. 5
- [36] Bin Sheng, Ping Li, Yuxi Jin, Ping Tan, and Tong Yee Lee. Intrinsic Image Decomposition with Step and Drift Shading Separation. *IEEE Transactions on Visualization and Computer Graphics*, 26(2):1332–1346, 2020. 2
- [37] S. Song and R. Qin. A NOVEL INTRINSIC IMAGE DECOMPOSITION METHOD TO RECOVER ALBEDO FOR AERIAL IMAGES IN PHOTOGRAMMETRY PROCESSING. In *ISPRS Annals of the Photogrammetry, Remote Sensing and Spatial Information Sciences*, pages 23–30. Copernicus GmbH, 2022. 2, 4
- [38] Shuang Song and Rongjun Qin. A general albedo recovery approach for aerial photogrammetric images through inverse rendering. *ISPRS Journal of Photogrammetry and Remote Sensing*, 218:101–119, 2024. 2, 3, 4, 1
- [39] Zhou Wang, A.C. Bovik, H.R. Sheikh, and E.P. Simoncelli. Image quality assessment: From error visibility to structural similarity. *IEEE Transactions on Image Processing*, 13(4): 600–612, 2004. 5
- [40] Chenfei Wu, Jiahao Li, Jingren Zhou, Junyang Lin, Kaiyuan Gao, Kun Yan, Sheng ming Yin, Shuai Bai, Xiao Xu, Yilei Chen, Yuxiang Chen, Zecheng Tang, Zekai Zhang, Zhengyi Wang, An Yang, Bowen Yu, Chen Cheng, Dayiheng Liu, Deqing Li, Hang Zhang, Hao Meng, Hu Wei, Jingyuan Ni, Kai Chen, Kuan Cao, Liang Peng, Lin Qu, Minggang Wu, Peng Wang, Shuting Yu, Tingkun Wen, Wensen Feng, Xiaoxiao Xu, Yi Wang, Yichang Zhang, Yongqiang Zhu, Yujia Wu, Yuxuan Cai, and Zenan Liu. Qwen-image technical report, 2025. 7, 6
- [41] Yao Yao, Zixin Luo, Shiwei Li, Jingyang Zhang, Yufan Ren, Lei Zhou, Tian Fang, and Long Quan. BlendedMVS: A Large-scale Dataset for Generalized Multi-view Stereo Networks. *Computer Vision and Pattern Recognition (CVPR)*, 2020. 6, 3
- [42] Junyan Ye, Dongzhi Jiang, Zihao Wang, Leqi Zhu, Zhenghao Hu, Zilong Huang, Jun He, Zhiyuan Yan, Jinghua Yu, Hongsheng Li, Conghui He, and Weijia Li. Echo-4o: Harnessing the power of gpt-4o synthetic images for improved image generation. <https://arxiv.org/abs/2508.09987>, 2025. 7, 6
- [43] Ye Yu and William Smith. InverseRenderNet: Learning Single Image Inverse Rendering. In *Proceedings of the IEEE/CVF Conference on Computer Vision and Pattern Recognition*, pages 3155–3164, 2019. 1, 2
- [44] Ye Yu and William Smith. Outdoor inverse rendering from a single image using multiview self-supervision. *IEEE Transactions on Pattern Analysis and Machine Intelligence*, pages 1–1, 2021. 2
- [45] Zheng Zeng, Valentin Deschaintre, Iliyan Georgiev, Yannick Hold-Geoffroy, Yiwei Hu, Fujun Luan, Ling-Qi Yan, and Miloš Hašan. RGB↔X: Image decomposition and synthesis using material- and lighting-aware diffusion models. In *ACM SIGGRAPH 2024 Conference Papers*, pages 1–11, New York, NY, USA, 2024. Association for Computing Machinery. 1, 2, 5, 6
- [46] Richard Zhang, Phillip Isola, Alexei A. Efros, Eli Shechtman, and Oliver Wang. The Unreasonable Effectiveness of Deep Features as a Perceptual Metric. In *Proceedings of the IEEE Conference on Computer Vision and Pattern Recognition*, pages 586–595, 2018. 5
- [47] Jingsen Zhu, Fujun Luan, Yuchi Huo, Zihao Lin, Zhihua Zhong, Dianbing Xi, Rui Wang, Hujun Bao, Jiayang Zheng, and Rui Tang. Learning-based inverse rendering of complex indoor scenes with differentiable monte carlo raytracing. In *SIGGRAPH asia 2022 conference papers*, Daegu, Republic of Korea, 2022. Association for Computing Machinery. Number of pages: 8 tex.address: New York, NY, USA tex.articleno: 6. 2, 5

# Olbedo: An Albedo and Shading Aerial Dataset for Large-Scale Outdoor Environments

## Supplementary Material

### A. Image Processing Details

This section expands the description of our aerial image preprocessing pipeline in Sec. 3. We detail how RAW images are decoded, converted to linear RGB EXRs, georegistered, and downsampled before albedo–shading decomposition.

**Acquisition setup.** All aerial images are captured using a DJI Phantom 4 Pro V2.0 with the built-in 1-inch CMOS camera. We record *only* RAW Digital Negative (DNG) files; in-camera JPEGs are not used anywhere in our pipeline. First, JPEGs apply vendor-specific tone curves, camera response functions (CRFs), and other non-linear image signal processing that destroy the linear relationship between scene radiance and pixel values. Second, the JPEG images have been undistorted with the built-in coefficients, which can conflict with the radial–tangential distortion model used in photogrammetry software. Third, RAW DNGs provide a higher bit depth (12 or 14 bits per channel) compared to JPEGs (8 bits per channel), which helps preserve subtle details in shadows and highlights that are crucial for accurate albedo–shading decomposition, as illustrated in Fig. 1.

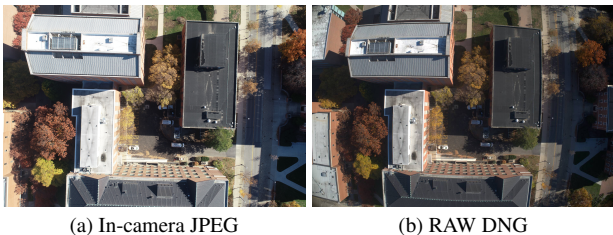


Figure 1. Comparison between in-camera JPEG (a) and RAW DNG (b) from the same scene. The JPEG image exhibits visible artifacts such as color clipping in highlights, loss of shadow details, and posterization effects due to aggressive compression and tone mapping. In contrast, the RAW DNG preserves a wider dynamic range and more accurate color representation, which are essential for reliable albedo–shading decomposition.

**RAW decoding and linearization.** We decode all DNGs using OpenImageIO (OIIO) configured to return values in the camera’s linear RAW color space:

- `oiio:RawColor = 1` to request RAW sensor-space values without applying DNG color transforms.
- `raw:ColorSpace = Linear` to ensure the output is linear with respect to sensor radiance.

No in-camera JPEG pipeline, tone mapping, gamma curve, or camera response function (CRF) is applied at any stage of our preprocessing. We use OIIO’s demosaicing and white-

balance handling as provided by its RAW interface, while keeping the output in a linear radiometric scale.

**Conversion to EXR.** All RGB, albedo, and shading images that we release are stored as OpenEXR (EXR) files in linear color space:

- The RGB EXRs are obtained directly from the RAW decoding described above.
- The albedo and shading EXRs are generated by running the intrinsic decomposition method [38] on the downsampled linear RGB images.
- No gamma correction, tone mapping, or sRGB transfer function is baked into these EXRs.

sRGB is used only for visualization in the paper (figures) and for low-resolution preview thumbnails. Any user wishing to work in display space should explicitly convert the provided EXRs using a standard sRGB transfer function.

**Camera calibration and geometry.** Camera intrinsics, poses, and 3D geometry are estimated using the commercial photogrammetry software Bentley iTwin Capture<sup>3</sup>. To handle multiple flights of the same area, we use virtual ground control points to align different captures into a single, georegistered coordinate system. The virtual GCPs are created by manually selecting keypoints on prominent, static features visible across different flights (e.g., building corners, road intersections). iTwin Capture uses these points to optimize camera poses and align the reconstructed models into a common world coordinate system with real-world scale and orientation. A uniform coordinate system allows us to reproject from one image to another using depth maps for cross-view consistency checks and change detection. We provide the calibrated camera intrinsics and extrinsics for each image in the dataset. The reconstructed 3D geometry is exported as a textured mesh in OBJ format.

### B. Image Decomposition Method

We adopt an outdoor illumination model proposed by Song et al. [38] to describe the shading conditions in outdoor images. We start from the rendering equation in Eq. (1). The illumination consists of a directional component from solar radiation and a spherical component from the sky.

$$L_o(\omega_o) = L_e(\omega_o) + \int_{\Omega} L_i(\omega_i) f_r(\omega_i, \omega_o) \langle \omega_i \cdot \mathbf{n} \rangle^+ d\omega_i \quad (1)$$

<sup>3</sup><https://www.bentley.com/software/itwin-capture/>

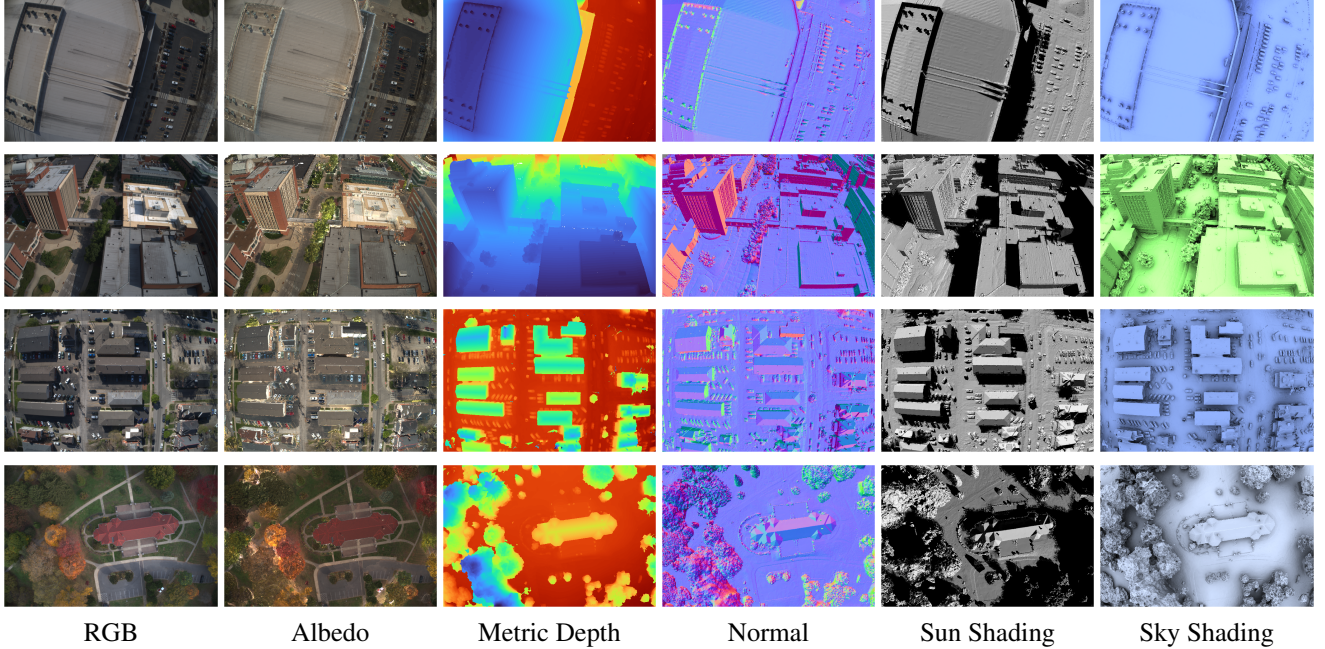


Figure 2. Additional examples from the Olbedo dataset. Rows from top to bottom: arena, office, residential, and park scenes.

where  $L_o(\omega_o)$  is the outgoing radiance in direction  $\omega_o$ ,  $L_e(\omega_o)$  is the emitted radiance,  $L_i(\omega_i)$  is the incident radiance from direction  $\omega_i$ ,  $f_r(\omega_i, \omega_o)$  is the bidirectional reflectance distribution function (BRDF),  $\mathbf{n}$  is the surface normal, and  $(\cdot)^+$  denotes the positive-part function, i.e.,  $\max(0, \cdot)$ .

For diffuse, non-emissive surfaces, the rendering equation simplifies to

$$L_o(\omega_o) = \int_{\Omega} L_i(\omega_i) \langle \omega_i \cdot \mathbf{n} \rangle^+ d\omega_i. \quad (2)$$

$$\text{where } L_i(\omega_i) = L_{sun}(\omega_i) + L_{sky}(\omega_i). \quad (3)$$

The incident radiance  $L_i(\omega_i)$  can be further decomposed into sun and sky components as Eqs. (4) and (5).

$$L_{sun}(\omega_i) = \psi_{sun} \cdot V_{sun} * \delta(\omega_i - \theta_{sun}), \quad (4)$$

where  $\psi_{sun}$  is the solar radiance constant,  $V_{sun}$  is the visibility function for the sun (1 when the sun is visible, 0 otherwise), and  $\delta$  is the Dirac delta function centered at the sun direction  $\theta_{sun}$ .

$$L_{sky}(\omega_i) = \psi_{sky} \cdot \mathcal{G}(\omega_i - \theta_{sun}) \cdot V_{sky}(\omega_i), \quad (5)$$

where  $\psi_{sky}$  is the sky radiance constant, and  $\mathcal{G}$  is a spherical function modeling the sky light distribution, with its lobe centered at the sun direction  $\theta_{sun}$ . To simplify the model in practice, we use a uniform sky distribution, i.e.,  $\mathcal{G}$  is constant over the visible sky.  $V_{sky}$  is the sky visibility function; it

is defined on the hemisphere above the horizontal plane, matching the support of the sky light distribution.

$$\phi = \frac{\psi_{sun}}{\psi_{sky}}. \quad (6)$$

We can integrate the sun and sky components separately and rearrange them as normalized shading components corresponding to the image formation model in Eq. (1) of the main paper (see Sec. 3):

$$\begin{aligned} S_{sun} &= V_{sun} \cdot \langle \mathbf{n}, \theta_{sun} \rangle^+, \\ S_{sky} &= \int_{\Omega} V_{sky}(\omega_i) \cdot \mathcal{G}(\omega_i - \theta_{sun}) \cdot \langle \mathbf{n}, \omega_i \rangle^+ d\omega_i. \end{aligned} \quad (7)$$

In Fig. 2, we present additional data samples spanning multiple scenes and modalities from the *Olbedo* dataset.

### C. Example of Confidence Mask

The confidence binary mask (shown in Fig. 3) is generated based on the criteria outlined in Sec. 3 of the main paper. It identifies regions in the albedo-shading decomposition where the estimates are considered reliable. High-confidence areas typically correspond to well-lit, textured surfaces with minimal shadows or specular highlights, while low-confidence areas may include sky regions, shadowed areas, or surfaces with ambiguous reflectance properties.

During fine-tuning of Intrinsic Image Diffusion [21], RGB $\leftrightarrow$ X [45], and Marigold-IID-Appearance [20], we apply the binary confidence mask to restrict the latent loss to valid regions, ensuring that each model learns only from reliable ground truth albedo.



Figure 3. Example of confidence mask for albedo-shading decomposition. Blue regions indicate high confidence, while dimmer regions indicate low confidence.

## D. Multi-view Consistent Retexturing

We apply the predicted albedo obtained from our fine-tuned  $\text{RGB} \leftrightarrow \text{X}$  model to retexture the reconstructed 3D models. Experiments are conducted on both a self-collected UAV dataset featuring buildings with fine structural details, and the publicly available BlendedMVS dataset [41] containing a variety of landscape types. As shown in Fig. 4 and Fig. 5, the retextured models exhibit a consistent appearance across all scenes, with most shading effects effectively removed compared to the original RGB-textured models. Notably, the retextured models preserve fine texture details—for example, building roof patterns and road markings remain clearly visible. These visualizations highlight the advantage of albedo recovery: data acquisition becomes less constrained by lighting conditions, and the albedo-based textures further enable flexible downstream applications such as relighting and material editing.

## E. Additional Relighting Renders

We provide additional visual comparisons in Fig. 6 across a diverse set of outdoor scenes. Each scene is rendered using both the original RGB texture and the recovered albedo texture. The examples span a wide range of structural geometries, surface materials, vegetation densities, and illumination conditions, including strong directional sunlight, partially occluded skylight, overcast weather, rainy environments, and nighttime lighting. Across all scenarios, the RGB-textured models exhibit baked-in shading effects. In contrast, the albedo-textured models consistently suppress these shading artifacts and produce spatially coherent, radiometrically stable appearances while preserving high-frequency material details. These results demonstrate that our approach generates albedo textures substantially more suitable for downstream rendering, relighting, and weather-agnostic asset creation.

## F. Additional Segmentation Results

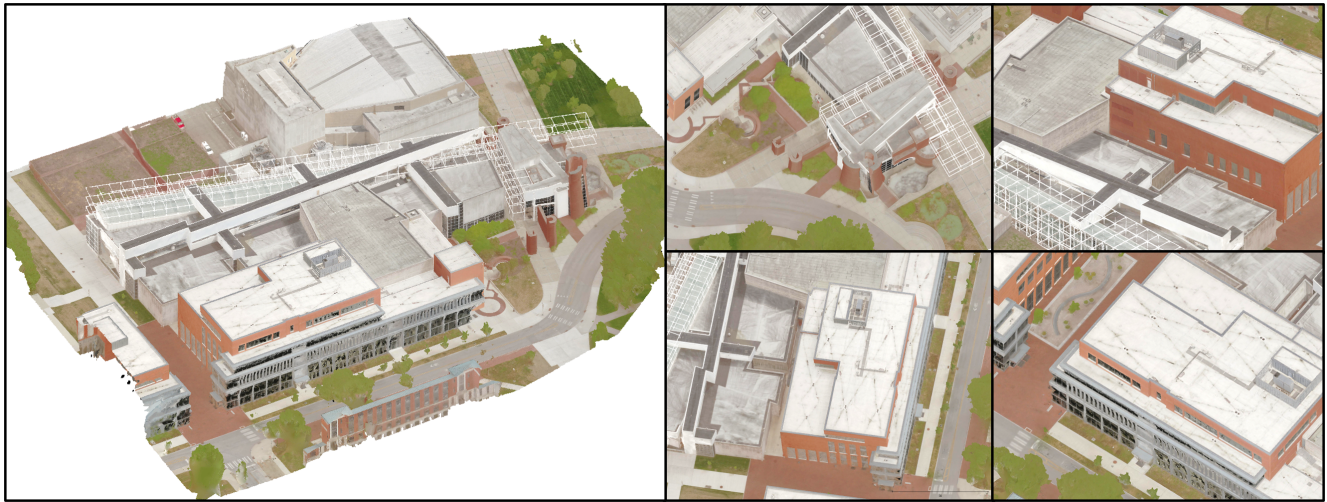
We provide additional qualitative segmentation examples using SAM [32] on both RGB and albedo images. As shown in Fig. 7, the segmentation performance is consistently better on albedo images across a broad range of outdoor scenes, particularly those containing complex cast shadows.

## G. Additional Material Editing Results

We include additional qualitative comparisons for the material editing task. The examples follow the setup described in Sec. 5 of the main paper, covering a variety of roof and façade materials as well as different target colors. As shown in Fig. 8, our approach consistently produces better editing results, particularly in terms of illumination handling and detail preservation.

## H. Additional Scene Change Analysis Results

Finally, we show more examples of lighting-invariant scene change analysis using the parking-lot surveillance dataset [17]. Each row in Fig. 9 corresponds to a different time step and demonstrates how albedo differencing suppresses illumination-induced changes while isolating true scene differences. These results highlight the advantages of using albedo representations to reduce appearance and lighting discrepancies in multi-temporal data, which is essential for robust change detection.



(a) Campus scene.



(b) BlendedMVS scenes.

Figure 4. Retextured models using recovered albedo images from the fine-tuned RGB $\leftrightarrow$ X.



(a) RGB-textured models.



(b) Albedo-ret textured models.

Figure 5. Comparison between RGB-textured models and albedo-ret textured models. Shading is largely removed while texture details are well preserved.

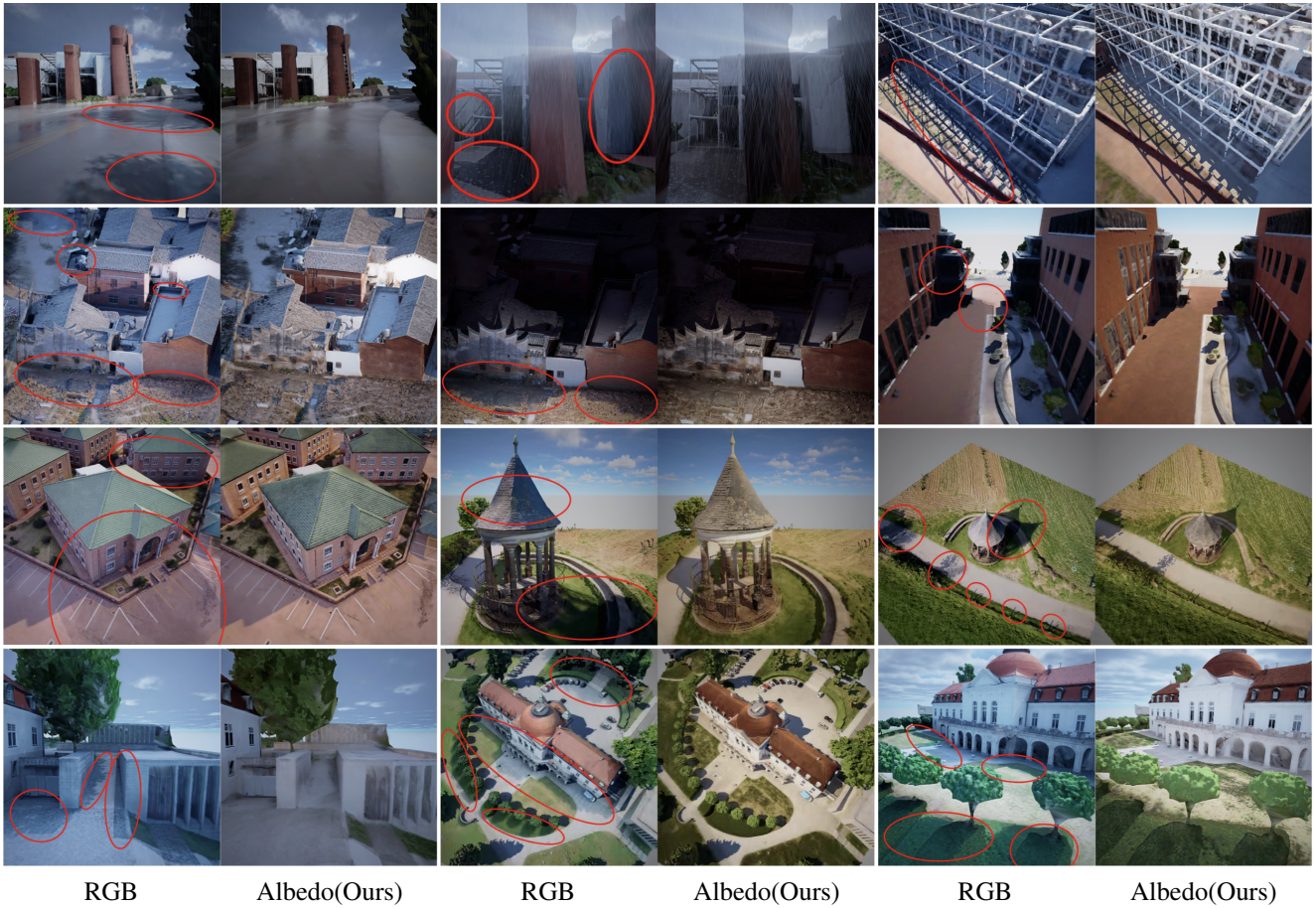


Figure 6. Additional visual comparisons between the RGB textures (left column of each pair) and our recovered albedo textures (right column of each pair) under novel lighting conditions. The scenes encompass diverse architectural styles, materials, and environmental conditions. Original textures contain baked-in lighting such as cast shadows, shading gradients, and environment-induced color shifts, whereas our albedo textures remove these illumination effects and retain only the intrinsic diffuse reflectance. These results highlight the stability and consistency of our method across varied outdoor environments.

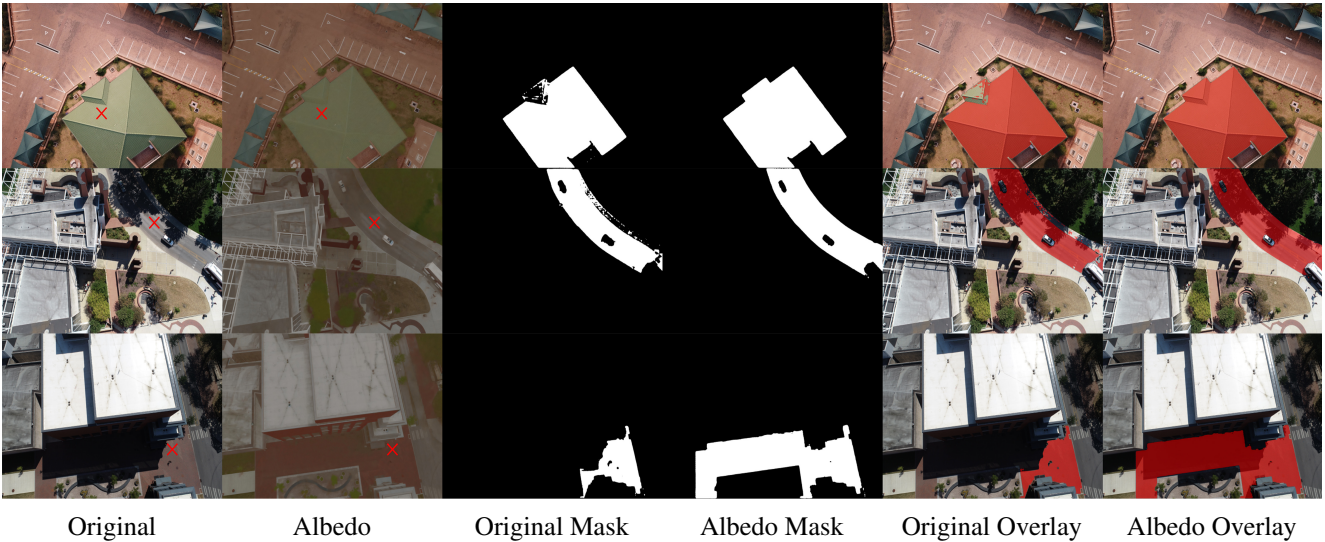
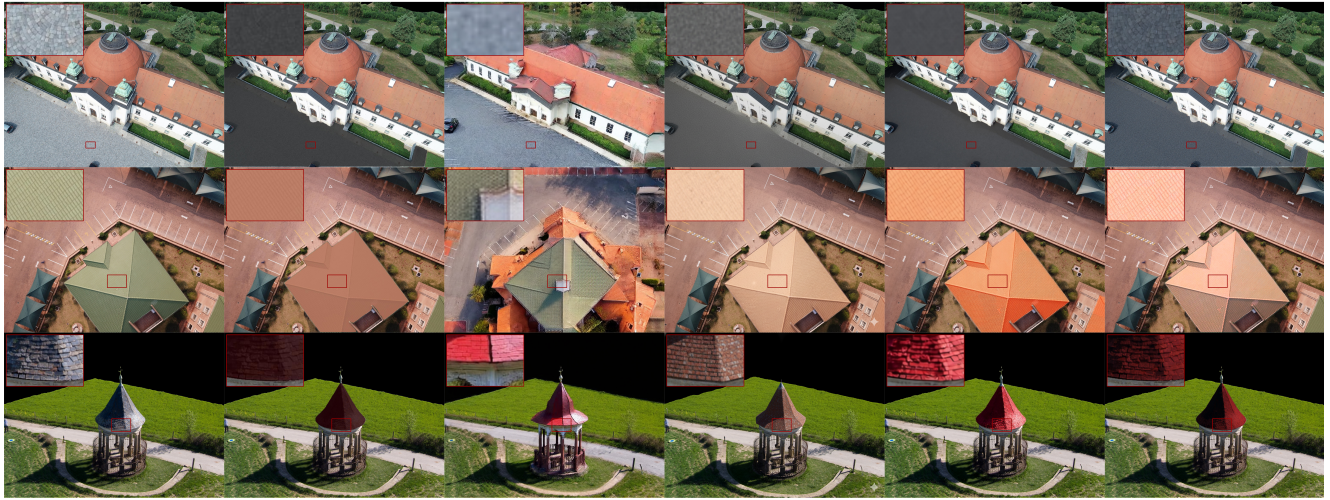
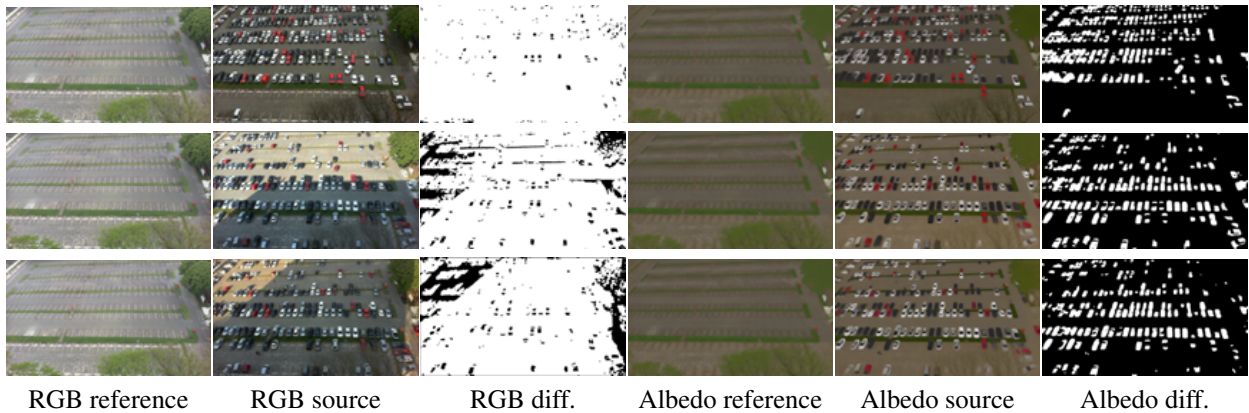


Figure 7. Additional segmentation results using SAM on RGB and albedo images. Each group of six images shows, from left to right: the RGB image, the corresponding albedo, the SAM mask predicted on RGB, the SAM mask predicted on albedo, and the two masks overlaid on the RGB image. Across diverse scenes, masks obtained from albedo remain more stable in shadowed regions and better preserve object boundaries than those obtained from RGB.



Original      Alpha-blending      FlowEdit+SD3      Nano Banana      Qwen Image Edit      Ours

Figure 8. Additional material editing results across multiple outdoor scenes. The target colors are  $\blacksquare$  (RGB: 40, 40, 40),  $\blacksquare$  (RGB: 190, 115, 92),  $\blacksquare$  (RGB: 40, 0, 0), respectively. For each scene, we compare naive alpha-blending, FlowEdit+SD3 [23], Nano Banana [42], Qwen Image Edit [40], and our albedo-based workflow. Our approach consistently preserves global illumination and fine structural details while achieving edits that closely follow the specified target colors.



RGB reference      RGB source      RGB diff.      Albedo reference      Albedo source      Albedo diff.

Figure 9. Additional examples of lighting-invariant scene change analysis with a fixed surveillance camera. Each row corresponds to a different time step. The left three columns show the RGB reference, RGB source, and naive RGB difference, while the right three columns show the corresponding albedo frames and albedo-based difference. Compared to RGB differencing, albedo differencing substantially reduces false positives caused by illumination variation and emphasizes true structural changes such as parked vehicles.